Complex REE zonations in metamorphic garnet reflect accessory mineral reactions

Niclas Hultin

Degree of Master of Science (120 credits)
with a major in Earth Sciences
45 hec

Department of Earth Sciences
University of Gothenburg
2020 B1081

Faculty of Science

UNIVERSITY OF GOTHENBURG

UNIVERSITY OF GOTHENBURG
Department of Earth Sciences
Geovetarcentrum/Earth Science Centre

Complex REE zonations in metamorphic garnet reflect accessory mineral reactions

Niclas Hultin

ISSN 1400-3821

B1081
Master of Science (120 credits) thesis
Göteborg 2020

Mailing address
Geovetarcentrum
S 405 30 Göteborg

Address
Geovetarcentrum
Guldhedsgatan 5A

Telephone
031-786 19 56

Geovetarcentrum
Göteborg University
S-405 30 Göteborg
SWEDEN

Table of Contents

Abstract 3
Sammanfattning 3
Introduction 4
Garnet zoning and the importance of REEs 4
Tectonic setting and regional geology 6
Methods 8
Microscopy, SEM and Raman 8
µ-Raman Spectroscopy mapping 8
LA-ICP-MS data acquisition and settings 8
Post processes 9
Sample description 9
Matrix 9
Garnet porphyroblasts 10
Results 11
Inclusions from RAMAN Spectrometry 12
Geochemistry of Garnets 13
Major element composition 13
Trace element composition 14
REEs 15
Other trace elements 17
Visualized inclusions 18
REE concentrations in the inclusion phases 21
Discussion 22
Major elements 22
Rare earth elements and trace elements 23
P-T path and mineral assemblages 24
Conclusions 26
References 27
Appendix 31

Abstract

A garnet from the Sesia Zone, NW Italy, was selected for Major and Rare Earth Element (REE) mapping, using LA-ICP-MS – a procedure previously not conducted at the Department of Earth Science at University of Gothenburg. The original inclusion assemblage of the garnet is preserved, and the mapping revealed two distinct changes in both garnet chemistry and inclusion assemblage, both which can be linked to the metamorphic development of the region. The onset and disappearance of REE bearing inclusions is mirrored in the garnet, as it showed fluctuating concentrations of REEs, while the mineral assemblage changed. The REEs are in this case the most valuable tool we have in terms of interpreting relict mineral reactions. If researched enough, the REEs on their own might yield enough information to interpret metamorphic events such as subduction episodes.

Key words: RARE EARTH ELEMENTS, REEs, GARNET, METAMORPHISM, LA-ICP-MS, SESIA ZONE

Sammanfattning

En granat från Sesia Zonen, NV Italien, valdes ut för spårämnesanalys medelst LA-ICP-MS, inklusive sällsynta jordartsmetaller (REE) och andra spårämnen. Detta är en analysmetod som inte tidigare använts på Institutionen för Geovetenskaper vid Göteborgs Universitet. Den ursprungliga inklusionssammansättningen i granaten är intakt, och karteringen visade på två distinkta förändringar i både geokemin och inklusionssammansättningen, vilka båda kan kopplas till den metamorfa utveckling som området genomgått. Både uppträdande och bortfall av REE-bärande inklusioner är speglat i granaten, då koncentrationen av REE fluktuerar samtidigt som inklusionernas sammansättning helt förändras. I detta fallet är REE det mest användbara verktyget för att kunna tolka relikt inklusionsförändring. Om dessa studeras tillräckligt kan de möjligen på egen hand ge tillräcklig information för att tolka metamorfa händelser så som olika subduktionsepisoder.

Nyckelord: SÄLLSYNTA JORDARTSMETALLER, GRANATER, METAMORFOS, LA-ICP-MS, SESIA ZONE

Introduction

Garnet is one of the most versatile minerals in metamorphic systems, with respect to thermodynamic and trace element modelling. Garnet is stable over a large pressure and temperature range – largely independent of rock type – and thus occurs in many metamorphic, metasomatic and magmatic environments. Garnet has a wide range of chemical compositions with complete solid solutions between most of its chemical endmembers and its major element composition well reflects the pressure (P), temperature (T) and chemical conditions (X) as well as the element transport kinetic properties of the host rock during growth (e.g., Berman, 1990; Chernoff and Carlson, 1997; Carlson, 2002; Caddick et al., 2010). Because diffusional element transport in garnet is very sluggish even at elevated temperatures (Chakraborty and Ganguly, 1992, Tirone et al., 2005) compositional growth zonations in garnet are very common (Hollister, 1966; Caddick et al., 2010). Information stored in these compositional variations makes garnet one of the most important recorders of geodynamic and element transport-processes in crust and mantle. Especially in subduction-related high pressure/low temperature rocks, such as eclogites, compositional growth zonations in garnet are commonly well preserved and display an important source of information about physico-chemical processes in the downgoing plate (e.g. Baxter and Caddick, 2013; Chopin, 1984; Konrad-Schmolke et al., 2006; Dragovic et al., 2012).

Garnet zoning and the importance of REEs

Garnets are nesosilicates with the general formula $X_3Y_2(ZO_4)_3$ where the different sites, X, Y and Z, display dodecahedral, octahedral and tetrahedral crystallographic coordination. For the most common garnets the X sites are filled with Ca^{2+}, Mg^{2+}, Fe^{2+}, Mn^{2+}. (Li et al., (2018), whereas the Y and Z sites are filled with Al^{3+} and Si^{4+}, respectively. The major element incorporation on the X site is predominantly controlled by pressure and temperature during garnet growth, whereas the substitution of Si for Al on the Z site is sensitive at ultra-high metamorphic pressures, which makes garnet a versatile mineral for geothermobarometry. Hence, garnet from different metamorphic zones appear to exhibit a variety of different major element zonation patterns, that are often interpreted in terms of P-T paths of the host rock utilizing thermodynamic forward models (Spear and Selverstone, 1989; Konrad-Schmolke et al., 2008b). Garnets from lower metamorphic grades also seem to be more zoned than those in high grade rocks with the assumption that higher temperatures favor increased diffusional relaxation of compositional growth zonations (Tracy et al., 1976; Kohn and Spear, 1991; Menard and Spear, 1989). However, the diffusional relaxation of pre-existing growth zonings is also used to determine metamorphic time scales if compared to modelled diffusion profiles (Chakraborty, 2006).

Garnet also incorporates a large number of trace elements, such as high field strength elements (HFSEs), Y and Cr as well as measurable quantities of Li, B, Sc, V, Co, Ni and K (Kotková and Harley, 2010; Hauri et al., 1994; Paquin and Altherr, 2001; Paquin et al., 2004), but rare earth elements (REEs) are undoubtedly the most often analysed and interpreted trace elements

in garnet (Moore et al., 2013). Especially with respect to the middle (Eu-Tb) to heavy (Dy-Lu) REEs garnet is the most important major phase in many rock types.

Rare earth elements and Yttrium are most often incorporated in garnet as trivalent ions substituting divalent ions at the (X) position. This bonding requires a coupled element substitution in order to balance the electron imbalance (Carlson et al., 2014), but the exact mechanism of this coupling is still uncertain. (Carlson, 2012).

Nevertheless are compositional REE variations in garnet interpreted in terms of scales of chemical equilibration and element transport properties in the host rock (Skora et al., 2006; Konrad-Schmolke et al., 2008b; Moore et al., 2013), they reflect fluid/melt-rock interaction (Jamtveit and Hervig, 1994), and they can be used to decipher major- and accessory phase breakdown during a rock's metamorphic evolution (Konrad-Schmolke et al., 2008b; Moyen, 2009). Furthermore, REE patterns in garnet enable reconstructions of P-T-time trajectories (Rubatto and Hermann, 2003; Whitehouse and Platt, 2003) and, regarding the Lu/Hf, Sm/Nd dating methods, enable absolute age and growth rate determinations (Griffin and Brueckner, 1980; Duchêne et al., 1997; Schmidt et al., 2008; Dragovic et al., 2012). Therefore, it is of utmost importance to quantify the processes that lead to the often complex REE zonation patterns in metamorphic garnet crystals.

The incorporation of REEs into the garnet crystal lattice are predominantly controlled by two major processes, the distribution of REEs between the garnet crystal and the matrix minerals as well as the availability of REEs at the garnets surface.

The REE distribution between garnet and matrix minerals is dominated by the fact that the ionic radius of the REEs decreases from the lighter to the heavier REEs, an electron orbital effect called lanthanide contraction. Hence, HREEs are preferentially incorporated into garnet over the LREEs as the smaller HREEs match better into the crystallographic site.

The availability of REEs at the garnet surface has a thermodynamic chemical equilibrium contribution, such as mineral reactions in the host rock and changing effective bulk rock composition EBC due to element fractionation (Konrad-Schmolke et al., 2008a), as well as a kinetic contribution, such as limited element transport in the interconnected transport matrix (ITM) and surface kinetics of the garnet crystal (Moore et al., 2013). This interplay between thermodynamic equilibrium, Rayleigh fractionation and kinetically controlled element transport enables recording of the rock's reaction path and its element transport properties, but complicates the interpretation of REE zoning patterns as the various effects on the REE patterns in garnet have to be evaluated.

In this contribution we demonstrate the effect of accessory mineral reactions in the host rock on the REE incorporation into garnet. Here its shown how a subduction related high pressure/low temperature rock that reactions among the titanium phases, namely titanite and rutile, and among phosphates, such as apatite and monazite leave a distinct REE pattern in the co-existing garnet that can be interpreted in terms of the rock's reaction path. The observations can serve as a general guide to the interpretation of reaction induced garnet REE patterns. However, the kinetic aspects of this problem are beyond the scope of this work and are discussed elsewhere (Spear and Daniel, 2001; Carlson, 2002; Skora et al., 2006; Kohn, 2009;).

2D major and trace element mapping, with µ-Raman mappings and detailed electron microscopy, are combined in order to correlate the mineral inclusion suite in a one cm large garnet porphyroblast from a high pressure/low temperature rock from the Western Alps. This combination of methods yields a plethora of information that was inaccessible before with single spot line measurements and should be a new standard method for the investigation of metamorphic garnets in the future.

Tectonic setting and regional geology

The studied garnet porphyroblast originates from a blueschist facies metabasite sampled in a southern tributary valley of the Aosta Valley in the Western Alps, Italy. The sample stems from an ancient Fe-Cu-mine, namely the Servette mine in the Saint Marcel valley, which is located in the central part of the Aosta Valley. The Saint Marcel valley is a 7 km long north south trending side valley connected to the larger east west trending Aosta valley near the small village of Saint Marcel. The geology of the valley is part of the Western Alpine Piemont zone and is described as a relict part of a dismembered section of Mesozoic Tethys Ocean (Martin and Tartarotti, 1989). Evidence supporting the claim of being of oceanic origin are mineral assemblages, isotope and geochemical data similar to that of present-day ocean floor-hydrothermal activity (Dal Piaz, 1999).

In the Saint Marcel valley the rock unit consists of two subdivisions and are described in short as oceanic basement, in the form of blueschist and eclogite facies meta-gabbros and hydrothermally altered metasediments. The units underwent polyphase high pressure/ low temperature (HP/LT) metamorphism during the Alpine orogeny, before getting partially retrogressed during exhumation through greenschist facies (Martin and Kienast, 1987).

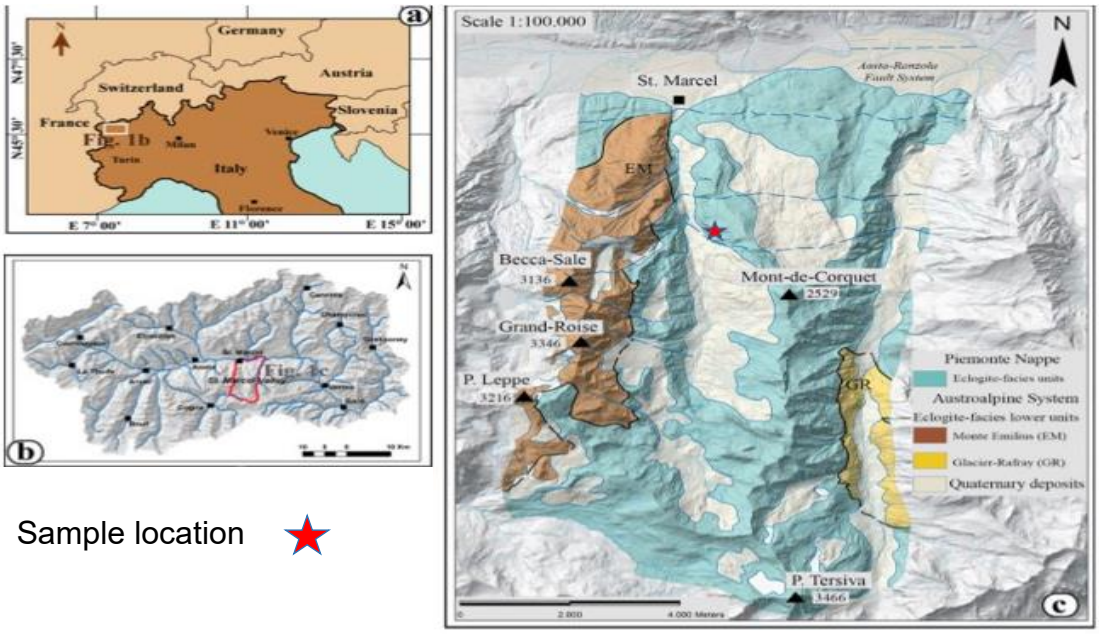

Figure 1 overview of sample location in the aosta valley NW italy. image from tartarotti et al. (2017)

The structural relationship between the meta-gabbro and metasediment units suggests that they have undergone contemporaneous metamorphic overprinting. This interpretation is derived from the correlation of polyphase deformation overprinting between the metabasites and the meta-sedimentary sequence above. (Martin and Tartarotti, 1989).

The pressure-temperature (P-T) path the rocks followed is interpreted to be hairpin-like, starting at about 350°C at 0.6 GPa and leading to peak metamorphic conditions of 550 ± 60°C at 2.1 ± 0.3 GPa (figure 2 interpreted from Martin et al., 2008). Low temperatures during the retrograde trajectory are indicated by the formation of chloritoid, crossite and talc (Martin and Tartarotti, 1998).

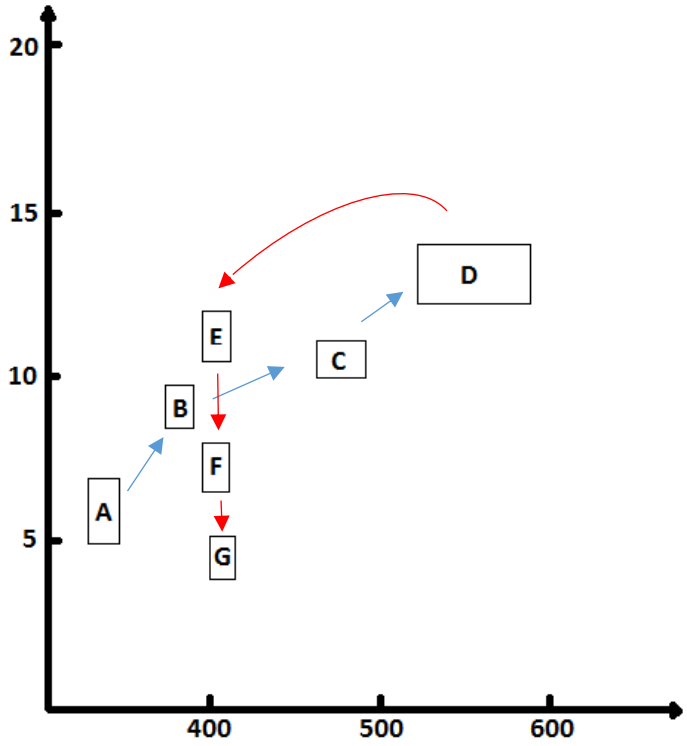

Figure 2 PT diagram of the metamorphic evolution of the Saint Marcel ophiolites, all areas are interpreted from mineral assemblages and mineral associations Figure and description are based on the work of Martin and tartarotti, (1989) A) – Inclusions of Titanite and Quartz in core of garnet. B) Formation of Chloritoid Glaucophane and chlorite in matrix. C) Almandine component of garnet increasing and same matrix mineralogy as B. D) Cummingtonite, Talc, magnetite and Albite in matrix. E) The retrograde step including Phengite microcline (+- Lawsonite), and Quartz. F) Quartz, Epidote, Chlorite (-+Talc), Albite. G) Same matrix as F with the addition of Actinolite. Blue arrows indicate the trajectory of the increasing PT path and the red arrows indicate the retrogression

Methods

Microscopy, SEM and Raman

To obtain a good overview in preparation for further analyzes a thoroughly characterization of major and accessory faces within the garnet as well as in the matrix both optical microscopy and a HITACHI S-3400N SEM (Scanning Electron Microscope) were used.

Electron microscopy was performed at the Earth Science Department (GVC) at the University of Gothenburg using a Hitachi S-3400N variable pressure scanning electron microscope (VP-SEM), that has a 200mm diameter sample chamber with the 5-axis eucentric motorized stage. The SEM has a manufacturer guaranteed maximum resolution of 4nm that can be reached for conducting samples. The tested resolution for non-conducting materials is in the order of 200nm. The samples were coated with carbon at GVC and subsequently stored under dry conditions until it was analyzed. The HITACHI S-3400N at GVC is equipped with an Oxford EDX spectrometer and one wavelength-dispersive crystal spectrometer. Additional detectors comprise a high contrast back scattered electron (BSE) detector, a secondary electron (SE) detector, a cathodoluminescence (CL) detector and an EBSD detector for crystal orientation measurements. User-friendly instrument control, data handling and analytical software runs on Windows®10 operating systems. Operating conditions were 6nA at an acceleration voltage of 20 kV. The beam size was in the order of 1µm. Quantitative analyses were done with an energy dispersive detector and calibrated with a Co standard. Dwell time was 60s for each element.

µ-Raman Spectroscopy mapping

The distribution of minerals was also found using Raman spectrometry, which is a useful tool in geosciences as it is a non-destructive method. This enables further investigation on the same area afterwards, which is often necessary (Tan and Li, 2019). Laser-induced Raman measurements were carried out at room temperature using a Horiba LabRam HR Evolution at the Earth and Environmental Science Department of the University of Gothenburg, Sweden. The samples were exited with an air-cooled frequency doubled 532nm Nd-YAG laser utilizing an Olympus 50× objective (numerical aperture = 0.9). The lateral resolution of the unpolarized confocal laser beam was on the order of 1 µm. Spectra were generated in the range of 100 to 2500 cm^{-1} utilizing a 600 grooves/cm grating and a thermoelectric cooling electron multiplier CCD including a front illuminated 1600x200 pixel chip. The spectral resolution on the polished sample was in the order of 1 cm^{-1}. The wavenumber calibration was done using the 520,7cm-1 Raman band on a polished silicon wafer with a wavenumber accuracy usually better than 0.5 cm^{-1}. Raman mappings were conducted with a spatial resolution of 5µm (laser beam was 1µm, line spacing 5µm) and a dwell time of 0.1s. Characteristic spectral windows for the different phases in the RGB mapping were 520-550 cm^{-1} (red), 900-920 cm^{-1} (green) and 1075-1110 cm^{-1} (blue).

LA-ICP-MS data acquisition and settings

The LA-ICP-MS trace element maps were obtained using an ESI 213NWR (TwoVol2) laser ablation system, connected to an Agilent 8800-QQQ ICP-MS located at the department of Earth Sciences, University of Gothenburg. Similar mapping procedures has previously been

conducted by a few other authors (Raimondo et al., 2017; Ubide et al., 2015; and George et al., 2018), but have previously not been tested at this department.

The mapping itself was performed on a garnet cast into epoxy and then mounted with a spring-loaded holder designed to hold these types of samples. The images were created by letting the laser ablate material in a rectangular shape, covering core to rim of the sample. The measurements were carried out in an atmosphere consisting of a mixture of. A spot size of 40µm with a repetition rate of 10 Hz; producing energy of 6.5J/cm^2 on target. The scan speed used were 40 µm/s with a line spacing of 1 µm to ensure total coverage of the sample.

The measurements were conducted in one continuous sweep, and standards were measured before and after the mapping. A total of 25 elements were measured for each line. The dwell time for each element were 0.5 second. The standards used here were the universal standard NIST 610 further described in (Pearce et al., 1997) and BCR-2G (Basalt, Columbia River) from the United States Geological Survey (Jochum et al., 2005) The total time of acquisition, for the area covering 7 by 4mm was 4.5 hours including the reference materials.

Spot analyses were also conducted on certain mineral inclusions to be able to accurately identify the variance of REEs in the inclusion assemblage. The spot size used, ranged from 10-25 micron depending on inclusions size. Analysis time were set to 60 seconds, and the same elements monitored during the mapping were also covered here, with the addition of La-Sm (LREE). Both NIST610 and BCR-2G were used as reference (inclusions measured includes allanite, titanite, apatite and monazite)

Post processes

Data reduction and filtering was performed using Iolite 3.6, an ad-on program for Igor-pro (WaveMetrix) developed at the isotope research center at the University of Melbourne (Paton et al., 2011). Data filtering and reduction are based on linear fit between the standards, measured before and after the mapping run. Background and noise from the original data were also corrected and/or removed for a smoother experience.

For quantification of values for each element, an internal standard of silica content in garnet (weight percent average of SiO_2) was used as reference. It is worth mentioning that the amount of silica in inclusions differ from the composition of garnet, and hence does not reflect the actual composition for all minerals. Because of this, the resulting maps yields a certain mismatch in concentration depending on how the silica content deviates between garnet and inclusions. The resulting maps are still a great way of showing internal differences for garnet and visualizes where changes in mineralogy and internal chemistry takes place.

For the spots, the NIST 610 was used to convert CPS to ppm, with internal standards varying depending on inclusion type (P for monazite and apatite, and Ca for titanite and allanite).

Sample description

Matrix

The sample is a fist-sized fine-grained albite-phengite-glaucophane-talc-chlorite-schist with up to cm-sized garnet porphyroblasts. The mineral assemblage found of the matrix consists mainly of chlorite, quartz, albite, glaucophane, minor chloritoid, talc and accessory pyrite, hematite as

well as rutile partially transformed to ilmenite. Actinolite and minor traces of paragonite are present as well.

The most abundant phase is chlorite which represents roughly 30-40% of the matrix (Fig 3A+ 3B). Glaucophane is mostly found as sub-hedral to euhedral crystals with a size of up to roughly 300 µm, spread throughout the matrix. They are almost always aligned which, together with chlorite, defines a penetrative foliation that is wrapping around the garnet porphyroblasts. The pyrites are abundant and vary in size, the largest crystals identified are roughly 250 microns in size.

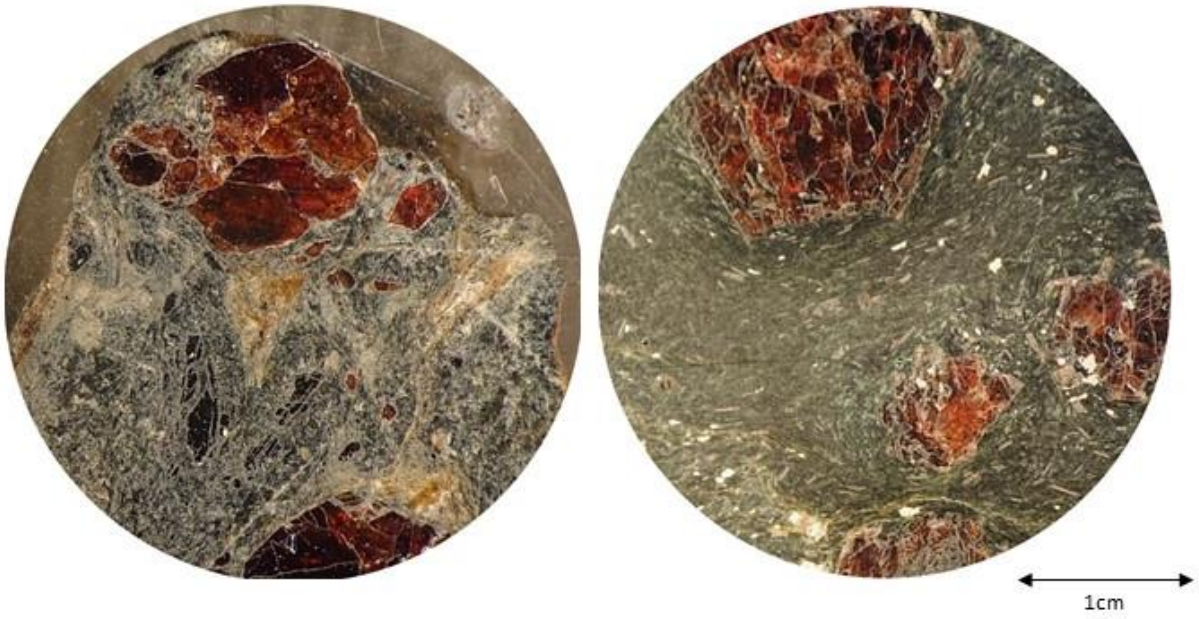

Figure 3A) to the left, matrix consisting of mainly chlorite (green) and of talc (yellow) with large and small pieces of garnet (red-brown), glaucophane (black) chloritoid (dark grey) one piece of actinolite (green-black) within talc area center of picture can be seen here. B) A piece of overwhelmingly chlorite (light green to green) matrix with abundant of pyrite (shiny yellow) with minor chalcopyrite, larger garnets (red-black) and abundant rods of ilmenite (grey) often aligned with the matrix itself

Garnet porphyroblasts

Garnet appears in the matrix mostly as euhedral grains with a bimodal size distribution, which is interpreted as a two-stage garnet growth during the monophase metamorphic evolution (Martin and Tartarotti, 1989). The smaller grains are between several hundred µm and a few millimeters, whereas the larger porphyroblasts are between one and three cm in size. The two garnet fractions from this locality have different chemical and mineralogical characteristics. The smaller grains are compositionally homogeneous and mostly inclusion free, whereas the larger fraction displays strong compositional core-to-rim zonations, inclusion-rich cores with varying inclusion assemblages and compositionally homogeneous and inclusion-poor rim overgrowths. Inclusions in the cores of the large porphyroblasts comprise quartz, titanite, zircon, allanite, epidote, apatite, rutile (in the outer parts of the cores) and ilmenite. The few inclusions in the rims of the large garnets are rutile, zircon, monazite, apatite and chlorite. (Martin and Tartarotti, 1989) interpret the small sized fraction of the garnets to be the same generation as the rim overgrowth of the large porphyroblasts.

Results

The euhedral garnet porphyroblast analyzed in this work corresponds to the large garnet fraction mentioned above and has a distinct inclusion-rich core zone that can be optically distinguished from a clear, inclusion-poor rim overgrowth (Fig. 5). The inclusion-rich part of the crystal makes approximately one half up to two thirds of the entire garnet radius and is also characterized by a larger number of randomly oriented brittle fractures. Fractures in the rims are fewer and are radially oriented (Fig. 5).

The inclusions in the inner core, corresponding to zone 1 in Figs. 5 and 6, consist predominantly of abundant large quartz inclusions and fine-grained titanite. Additionally, fine-grained (predominantly <15microns) fluorine apatite, xenotime and allanite is found. In the outer core region (zone 2 in Figs. 4, 5 and 6) xenotime and titanite are absent and instead titanite rutile and ilmenite appear as the Ti-phases together with quartz. Interestingly, ilmenite appears only at the transition between zone 1 and zone 2. Additionally, allanite and fluorine apatite are still present in zone 2.

Outside the line marked in red, which is the transition between zone 2 and 3, there is a drastic change in the inclusion abundance, in the inclusion assemblage as well as a change in the composition of the included phases. In the inner part of zone 3 the modal abundance of apatite is drastically decreasing, and it is practically absent in this region. Allanite disappears completely and monazite appears in zone 3. In the outer part of zone 3 apatite re-appears but its composition has changed towards chlorine apatite.

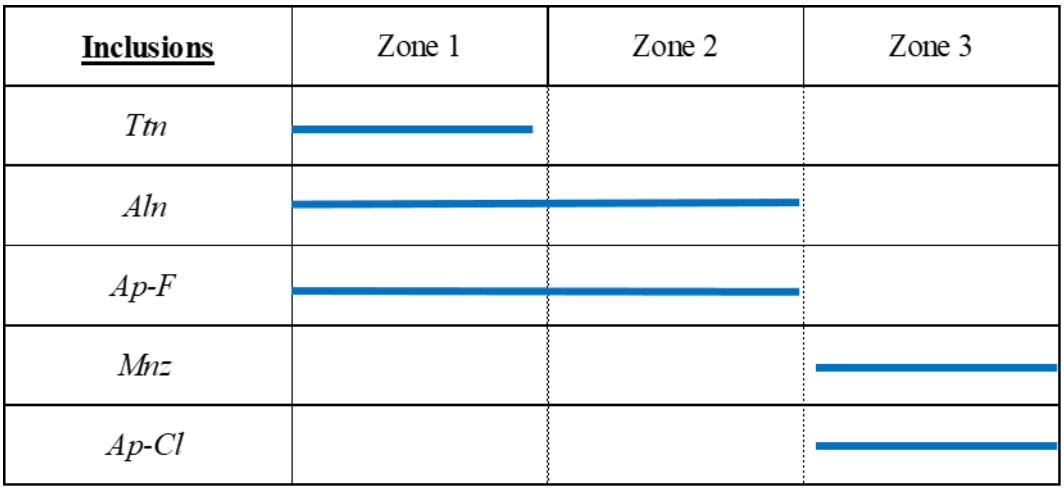

Figure 4. Summary of important REE bearing inclusion facies, and their location within the sample.

Zircons are found throughout the garnet occurring as small free euhedral crystals, predominantly found closer to the core, while occurring together with rutile and ilmenite as

clusters towards the rim. These clusters are rod-like and are aligned with the outer rim of the garnet. These aligned clusters can be followed around the entire sample.

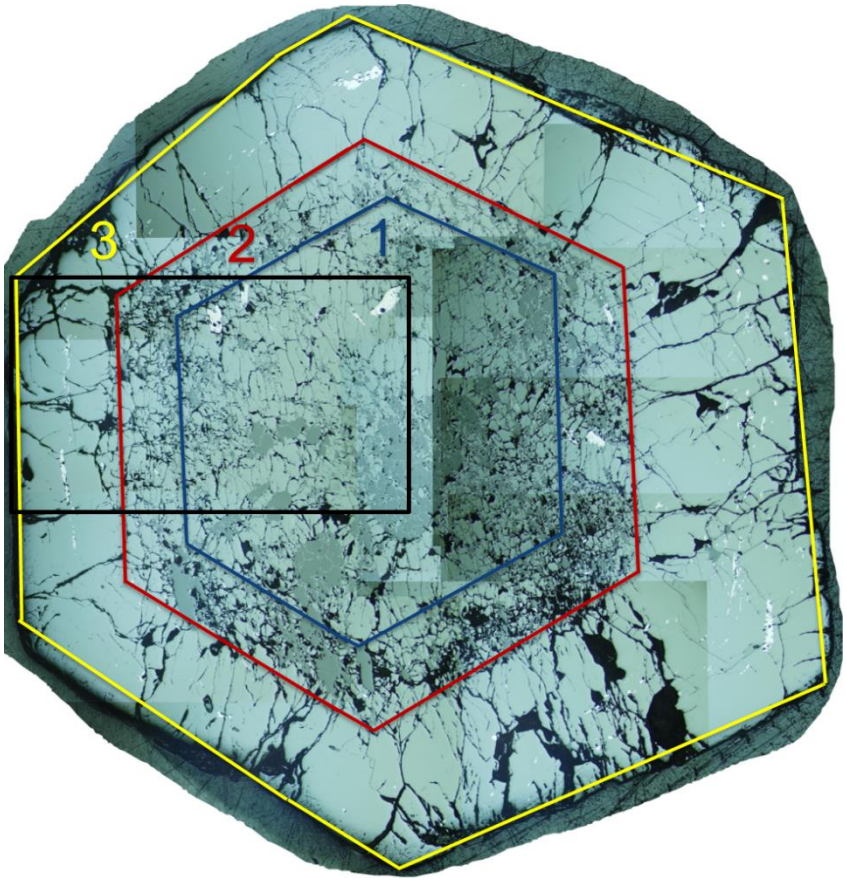

Figure 5. An overview image of the sample used in this study. Different zones are marked in color. ***Blue*** *– "core zone" reflects the outermost limit to where Titanite and xenotime are present.* ***Red*** *– "outer core" the boundary at which Apatites and Allanite/epidote disappear within the garnet,* ***Yellow*** *– "rim zone", the outermost part of garnet where there are less inclusions, generally displays a more homogeneous behavior. The black rectangle are the main study area chosen for LA- ICP-MS mapping.*

Inclusions from RAMAN Spectrometry

The change in the inclusion assemblage is evident in the µ-Raman mapping displayed in Fig. 6. In the inner core of the investigated garnet (green) large quartz (black) and small titanite (orange) as well as a few ilmenite (yellow) inclusions are abundant. At the transition from the inner to the outer core (between zone 1 and 2), marked by the blue line, titanite disappears entirely and fine-grained rutile (red) becomes the predominant Ti-phase throughout zone 2. Furthermore, in zone two the general abundance of inclusions decreases, and the garnet becomes less fractured. In the central part of zone 3, which is generally inclusion-poor, rutile inclusions become larger and more abundant and elongated rutile grains (together with smaller zircons that appear black in the mapping) are aligned parallel to the crystal faces. Allanite, monazite and xenotime inclusions are too small to be visualized in this overview mapping.

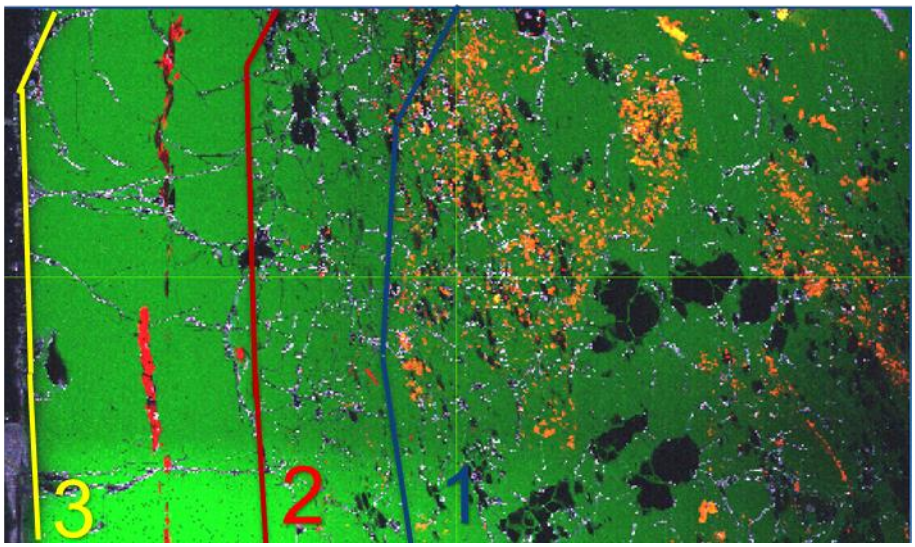

Figure 6. Difference in mineralogy shown by RAMAN spectrometry. The marked lines in color are the same as previously described.

Geochemistry of Garnets

Major element composition

The investigated garnet is almandine-rich with a compositional variance of Alm_{58-87} Py_{3-16} Grs_{2-26} Sp_{0-11} showing a typical prograde core to rim zonation of HP/LT garnets, indicated by a bell-shaped Sps pattern, increasing Py and Alm components and a decreasing Grs component (Fig. 7). The core of the garnet exhibits stable trends for all elements. At the transition between zone 1 and 2 almandine and pyrope start to increase and grossular decreases. Just after the boundary between zone 2 and 3 the almandine content reaches its maximum and the grossular content is approaching a minimum. In contrast, pyrope sees a steadier increase even after the transition between zone 2 and 3. Spessartine is almost absent outside zone 2.

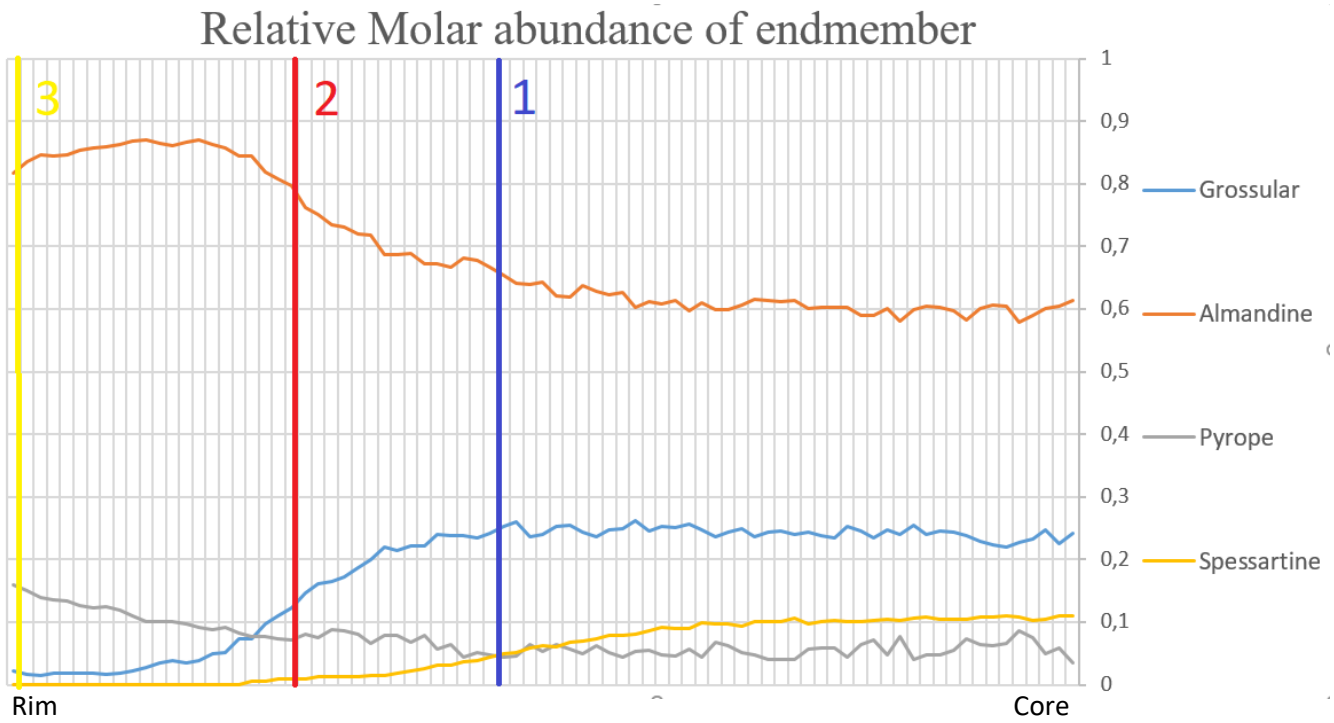

Figure 7. Molar abundance of the major components in garnet, with the marked zones of the garnet.

The major element maps seen below show at the beginning a smooth zoning with increasing trends for both Fe and Mg. Ca and Mn shows decreasing trends from core to rim. The patterns are patchy and sometimes irregular. Patches in the major element maps are mainly created by the abundance of inclusions, these patches can easily be seen in the Mn, Al, Fe, and Ca maps. (Fig 8). The map of Ca shows no data after roughly half the mapping, this is a consequence for exceeding the upper detection limit, which caused the detector to turn off. Despite the missing data, the Ca map still reveals Titanite inclusions as they have higher concentrations of Ca in their structure compared to the garnet. The Fe mapping displays a core to rim increase with some heavy enriched minerals. These three inclusions are Ilmenite that occur in the upper part of the mapped area. The major element-trends corresponds well to the observed data from the SEM profile described above.

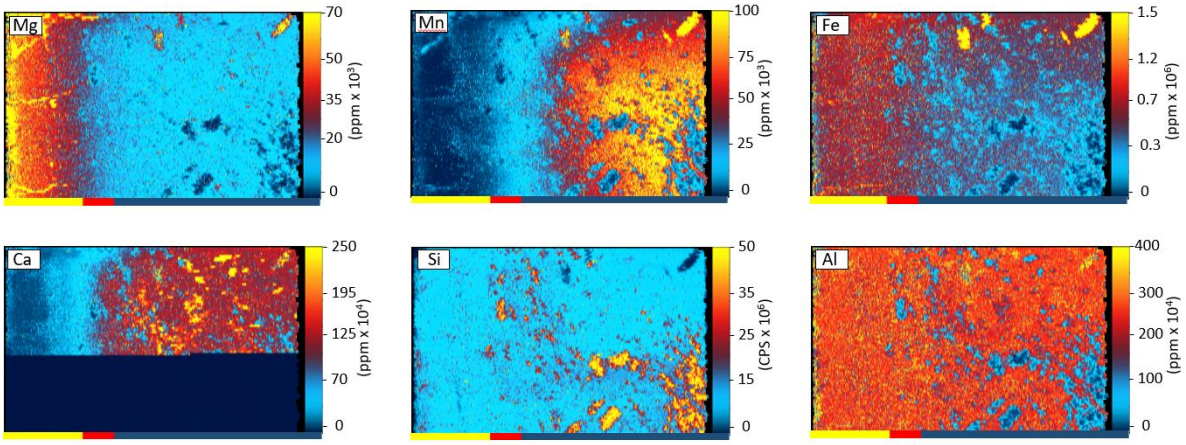

Figure 8. maps of the major elements included in the solid solution series of the most common garnets.

Trace element composition

In order to increase the amount of information about the trace element distribution within the garnet crystal we performed LA ICPMS trace element mappings across the central part of the large porphyroblast. The entire maps are given in the electronic supplementary material, whereas representative mappings of the left side of the crystal are shown in Figs. 8, 9 and 11. During analysis 19 trace elements were mapped (Ti, Sc, Y, V, Cr, P, Sr, Zr, Zn, Ga as well as 9 REEs (Eu-Lu). The lighter REEs were not measured because of the low concentrations in garnet, which resulted in values below the detection limit with the machine settings used for the mappings. It is notable that the smooth zonation of the major elements in garnet is clearly decoupled from most of the measured trace elements.

REEs

From the REE mappings (Fig. 9) it is evident that each element distribution is characterized by one or two concentric enrichment zones within the garnet crystal. Furthermore, some of the inclusions are enriched in certain elements, best visible in the Gd mapping that clearly highlights titanite and allanite inclusions. The overall concentrations, i.e. concentrations in garnet excluding the annuli, of all REEs is higher in the core and continuously decreasing towards the rim, where the concentrations of most REEs are close to the detection limit.

Most notable is the spatial distribution of the two enrichment zones. There is an inner annulus located between one half and two thirds of the entire garnet radius. The crest of this annulus coincides with the boundary between zone 1 and zone 2, which marks the disappearance of titanite and the appearance of rutile. This annulus is best visible in the HREE, but nearly absent in the Eu mapping. The enrichment zone is up to about 500µm wide and characterized by a continuous increase from core to the crest of the annulus, followed by a rapid decrease. The second enrichment zone is at about three quarter of the entire garnet radius, it is much narrower, the rise in concentration is less than in the first annulus and it best visible in the MREEs, but present in all REEs apart from Yb and Lu. Notably, this second annulus coincides with the boundary between zones 2 and 3, which marks the transition from allanite + F-apatite to monazite + Cl-apatite in the inclusion assemblage (see fig 12 for inclusion/reaction overview).

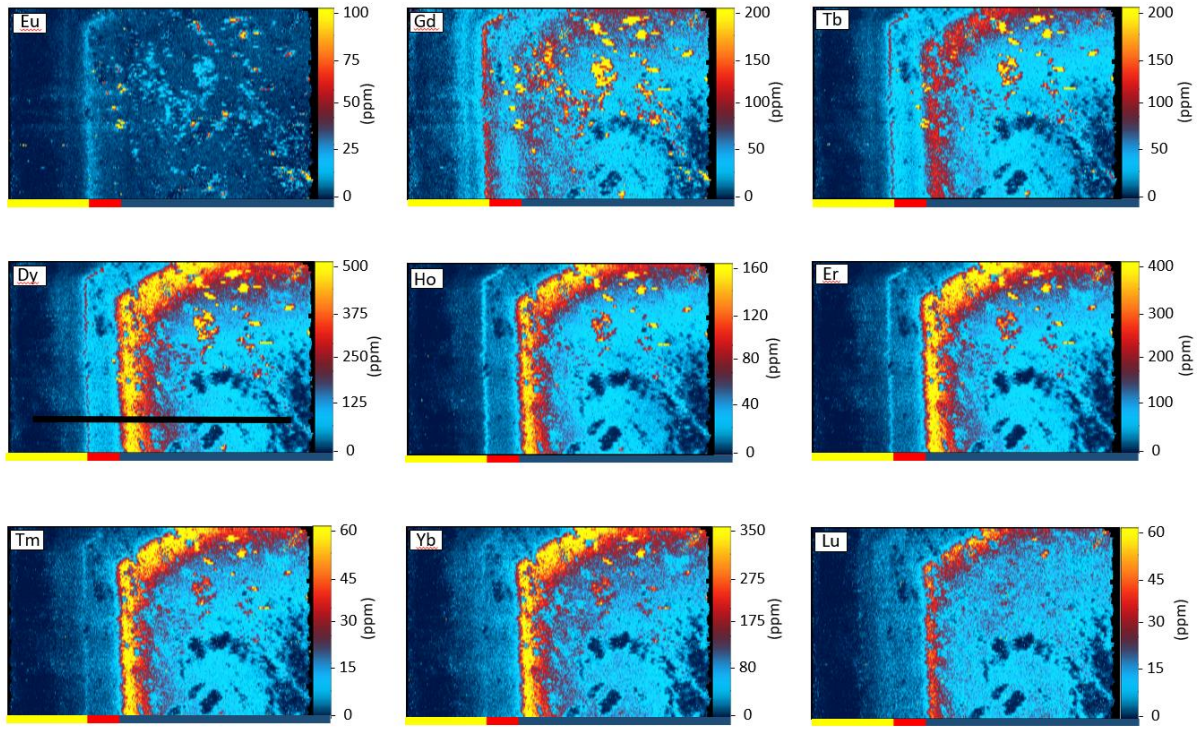

Figure 9. Mappings of the MREE Europium (Eu), Gadolinium (Gd), and Terbium (Tb). And the HREEs - Dysprosium (Dy), Holmium (Ho), Erbium (Er), Thulium (Tm), Ytterbium (Yb) and Lutetium (Lu). All maps have been adjusted so that the zonation of these elements is as clear as possible. Marked line in Dy image shows location from where profiles have been extracted.

The REE profiles shown in Fig. 10 are extracted from the mappings along the line shown in the Dy mapping. These profiles nicely show the continuous REE increase towards the crest of the inner annulus and the rapid decrease after the peak. This peak shape is also visible in the second annulus although it is less pronounced here. Furthermore, one can see clearly that the titanite- and allanite-out reactions coincide with these peaks (blue to red underlining guide). It is worth mentioning that the appearance of the first monazites coincides well with the crest of the second annulus, whereas the disappearance of the allanite and F-apatite occurs a few microns before the crest of the second peak.

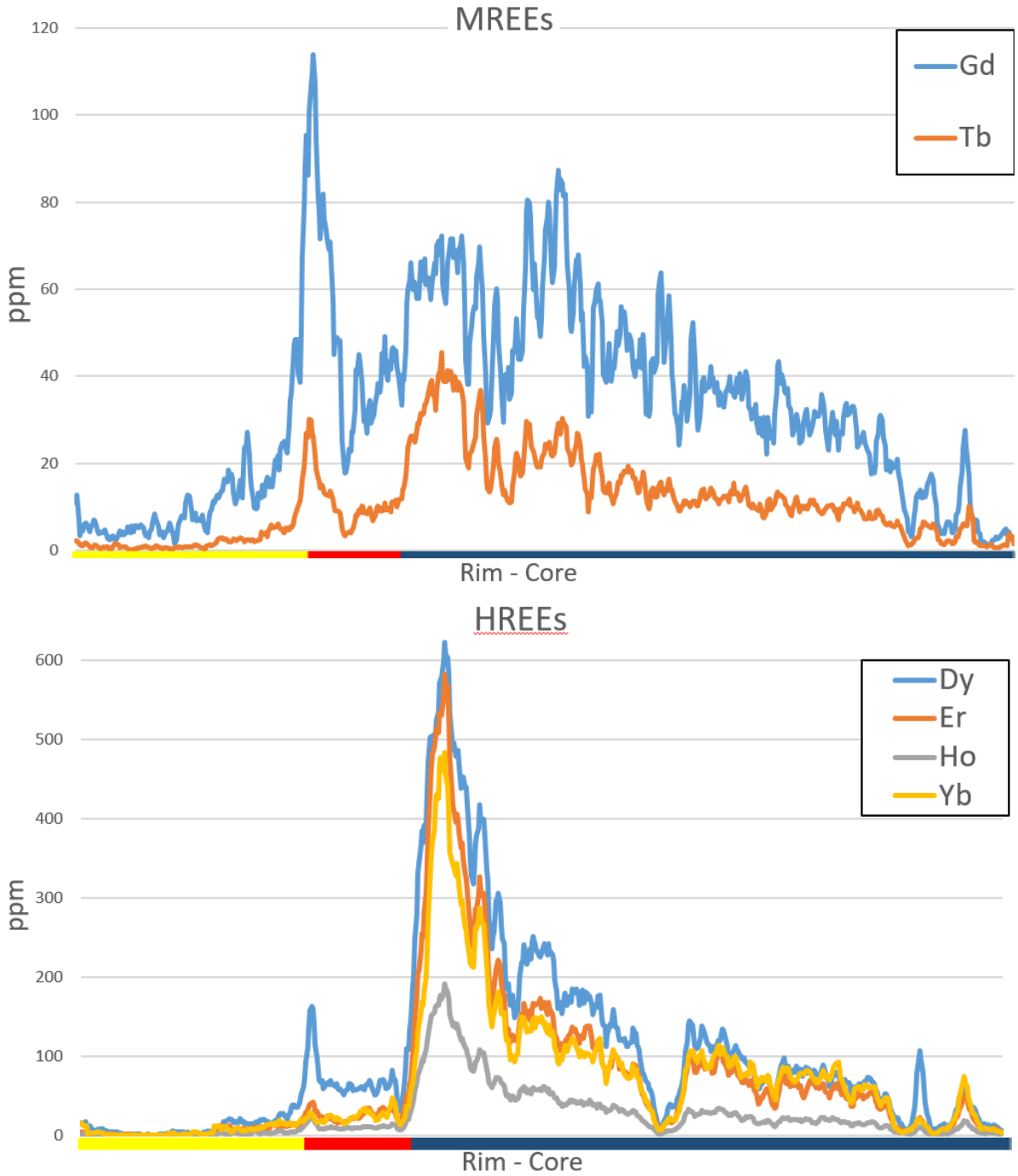

Figure 10. MREE and HREE profiles that displays the elements that shows the most pronounced change in concentration from core to rim.

Other trace elements

Phosphorous (P) shows no zonation inside the garnet core and inner rim but displays enrichment in P rich phases in the core compared to the rims. Towards the outer rim, approximately after the transition between zone 2 and 3, P seems to increase slightly within zone 3.

Vanadium and chromium (V and Cr) are enriched in inclusions such as rutile, ilmenite (yellow spots) and the larger titanite grains (red spots in the upper right corner). Chromium also displays an enriched zone just before the string of elongated rutile grains that are associated with smaller zircons (left side of the mapping), which can be seen in the maps of Cr, Ti and V. Additional mappings are found in the appendix (figure A1).

Scandium (Sc) and Yttrium (Y) are sometimes regarded as REE's because of their similar behavior. Here yttrium displays heavy enrichment in inclusions close to the core, and later two peaks of enrichment towards the rim. Sc is enriched in the core with a sudden decrease towards the rim with some minor fluctuations.

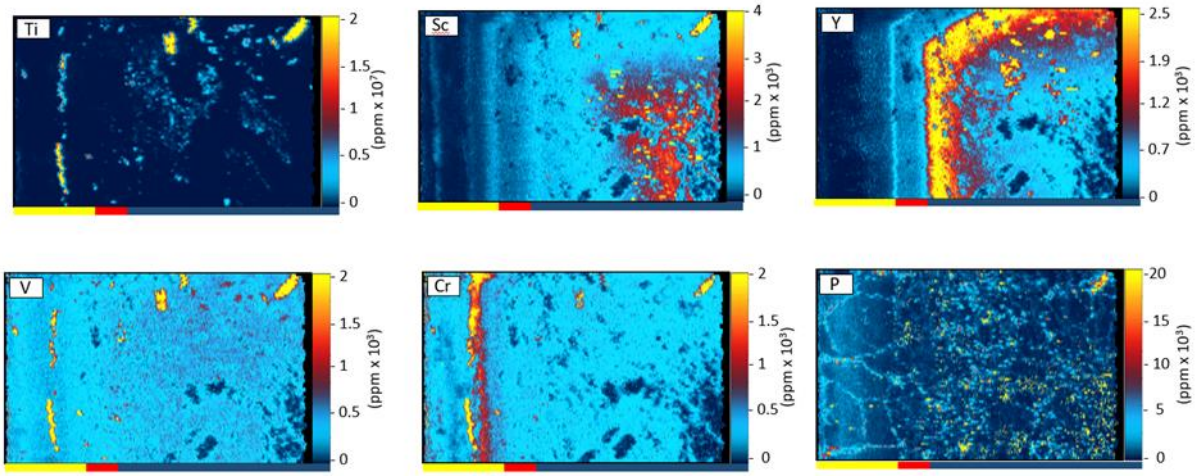

Figure 11. Major elements and trace elements incorporated in inclusions and the structure of garnet

Visualized inclusions

All inclusions in the sample have been carefully studied and identified. Figure 12 below shows each inclusion facies geographical location in the sample. The image combines knowledge acquired from the SEM, ICP-MS-MS and RAMAN. The background of the picture is an RGB composite, where red represents – titanium, green – Terbium and blue – Europium. The elements are hosted in inclusions and the garnet in various amounts and were selected because of the visual clarity it yields.

Despite Apatite being one of the most common minerals found in the garnet, it cannot be seen on this map due to the resolution of the image being coarser than the small <10 μm sized inclusions. However, they are abundant up to the dotted yellow line, where the abundance changes drastically and chemical signature changes from Fluorine carrying to Chlorine.

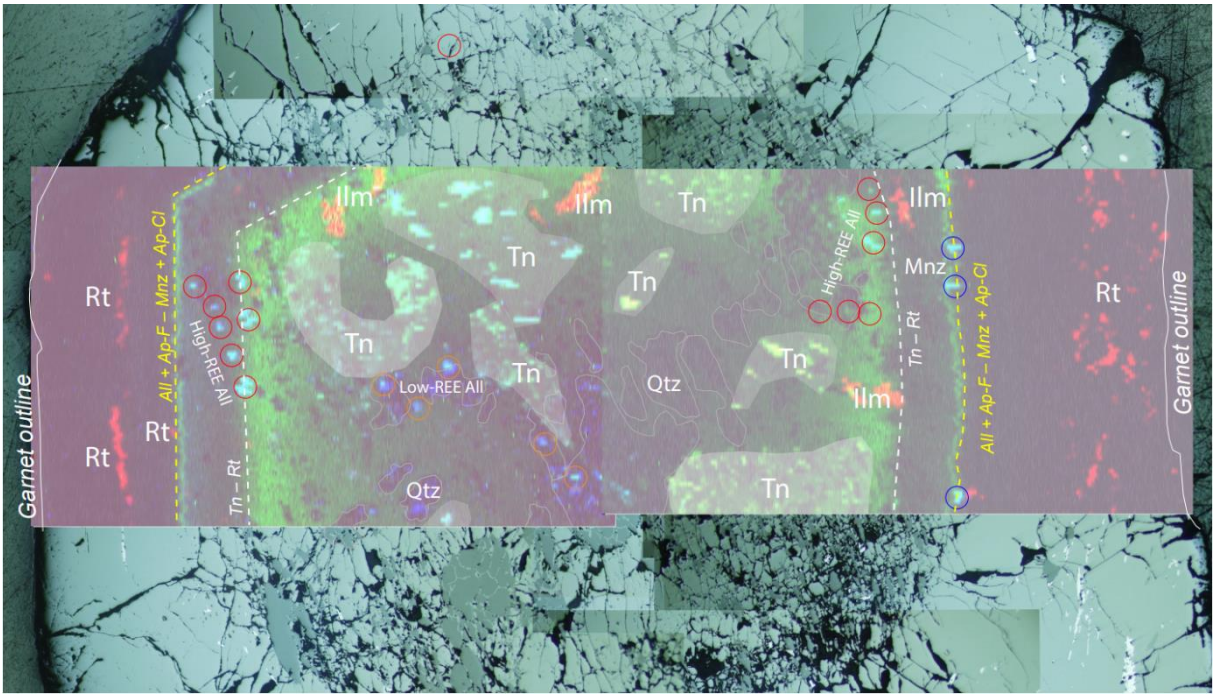

Figure 12. The inclusions and where they are located within the garnet sample.

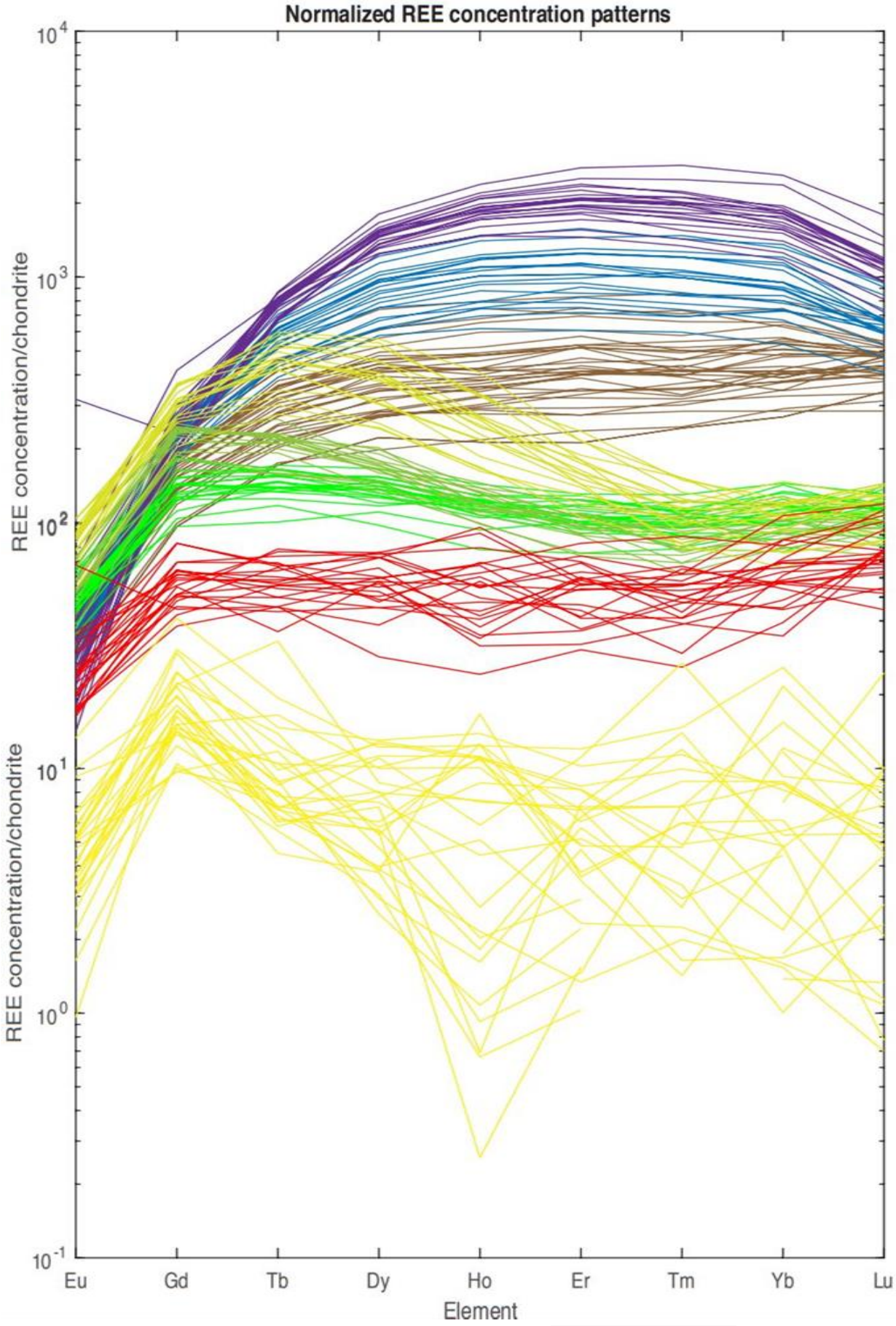

Figure 13. Normalized REE patterns normalized against chondrite from (Anders & Grevesse, 1989). The different colors represent "zone wise" core-rim variations.

So far it is shown that the garnet crystal exhibits a complex zoning with respect to the trace elements, particularly the REEs, and that these compositional variations correlate well with the observed change in the inclusion assemblage. Furthermore, it is notable that each of the different zones is characterized by differences in the REE patterns (Fig. 13). Based on the REE patterns an even more detailed picture of the REE distribution during prograde garnet growth can be given.

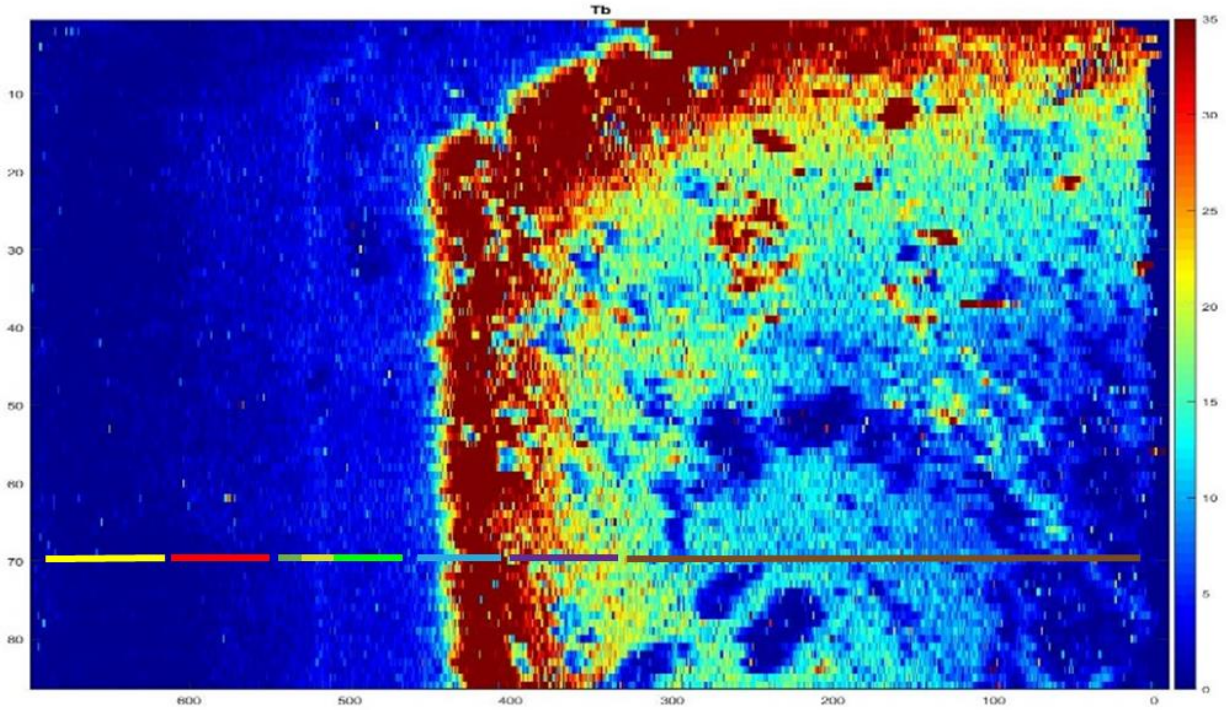

Figure 14. Overview of the different zones described in figure 13

The difference in REE patterns within the garnet varies from core to rim. Figure 13 displays the different patterns from several different portions of the garnet. The difference in concentration is explained from core to rim. The inner core of the garnet is represented the brown line and patterns in Figs. 13 and 14 and shows increasing REE concentrations till Gd and then a concentration plateau at about 5x10*2. In the steady slope region until the crest of the first annulus (purple line and patterns) the REE pattern becomes more concave-up curved as the concentrations of Tb to Lu increase, whereas the concentration of Eu and Gd stay constant. At the outward flank of the first annulus (light blue line and patterns) the concentrations of all HREE decrease so that the shape of the REE pattern is unchanged, but the concentrations decrease. The region between the two annuli has then a similar pattern than the inner core, but with slightly lower concentrations of the HREEs (dark green line and patterns). The next significant change in the REE pattern then occurs at the second annulus. Here the slope of the pattern becomes negative for the HREEs as the concentrations of Gd to Ho increase whereas Eu, Yb and Lu are constant (light green line and pattern). This circumstance is also evident from the REE mappings and profiles in Figs. 9 and 10. At the outer rim of the garnet REE concentrations are constant for the entire element suite apart from Eu (red and yellow lines and patterns). Comparison of the mappings, profiles and REE patterns suggests that the concentrations of all REEs are controlled by a combination of mineral reactions and superimposed element fractionation from the matrix into the garnet crystal.

REE concentrations in the inclusion phases

The REE concentrations of the different inclusion phases measured in the core, namely titanite, Allanite and Apatite, are shown in figure 15. All inclusions show enrichment in REEs relative to chondrite. All the REE patterns in the different inclusion phases, irrespective of their position within the garnet have a clear negative Eu anomaly. This circumstance reflects the fact that plagioclase was likely present during the entire P-T path of the sample (Tartarotti and Martin, 1989). Allanite has the steepest negative slope in the REE patterns with a strong preference for the LREE, whereas titanite and apatite have a convex upward pattern with a peak at Ho and Gd, respectively. Unfortunately, the grain sizes of the inclusions were too small for a thorough study so that a determination whether the shape of the REE pattern changes from garnet core to garnet rim. However, data from two apatite grains and titanite data extracted from the REE mappings suggest that inclusion phases close to the core have generally lower REE concentrations than those closer to the rim of the garnet crystal. Furthermore, apatite inclusions in the rims of the garnet (Fig. 16) also show a more fractionated pattern, such that the slope is steeper towards the HREEs.

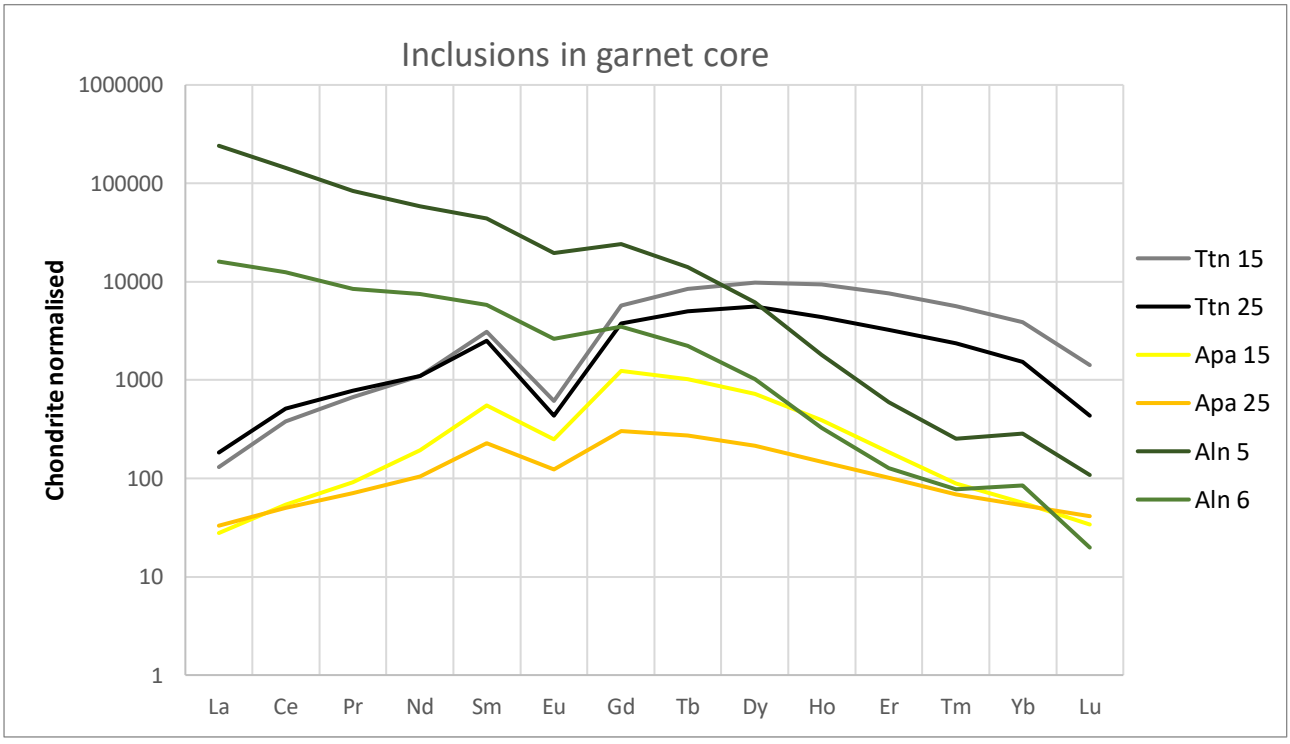

Figure 15. chondrite normalized values for the inclusions located in the core of the garnet. Chondrite values from (Anders & Grevesse, 1989)

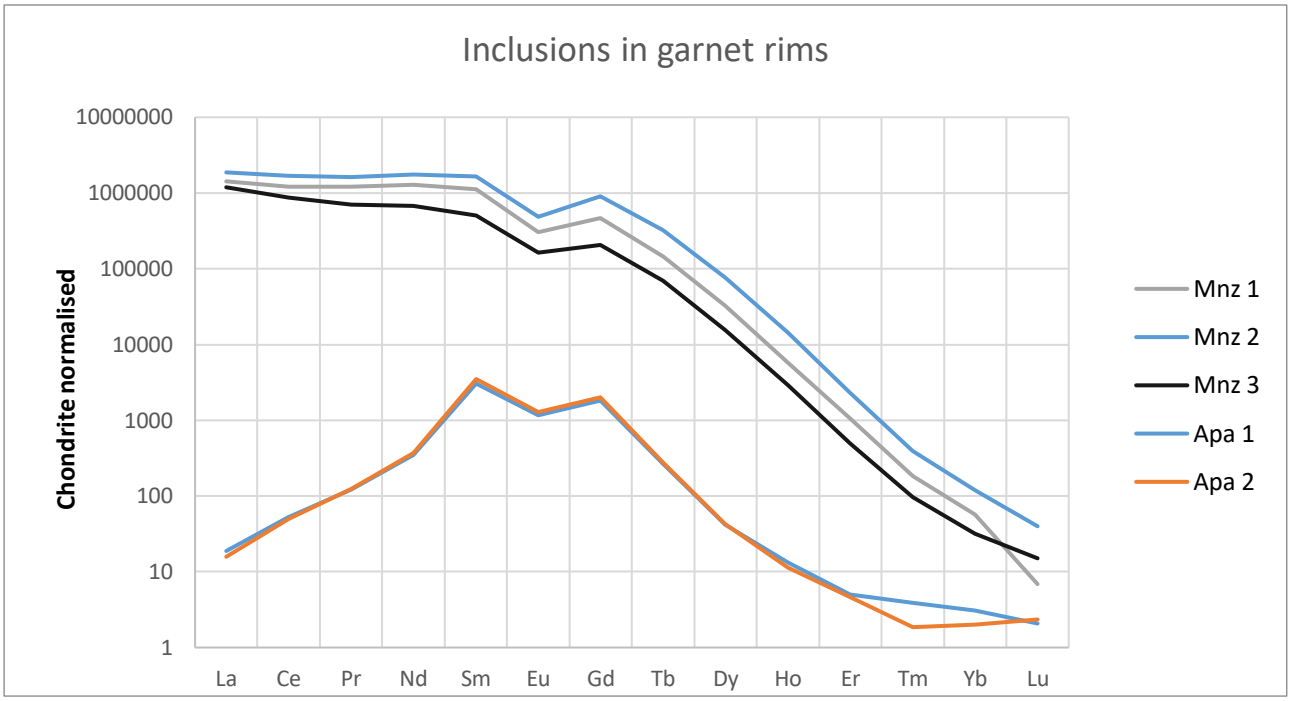

Figure 16 chhondrite normalised values for the inclusions located in the rim of the garnet. Chondrite values from Anders, E., & Grevesse, N. (1989)

Discussion

Our results from the comparison of inclusion phases, their compositions and positions within the garnet crystal with major and trace element mappings of the garnet porphyroblast points towards the assumption that the titanite-to-rutile transition as well as the transition from the assemblage allanite+F-apatite to monazite+Cl-apatite leaves characteristic traces in the REE composition as well as in the REE pattern of the host garnet. These findings make garnet more valuable for the determination of a rock's reaction path than before.

Major elements

All major elements incorporated in garnet shows a core- rim increase or decrease and are an excellent indicator for a prograde growth as mentioned by several authors.

Some of the major elements are excellent proxies for inclusions found throughout the garnet, and if possible, could also be used when mobile elements have been remobilized during a metamorphic event, in the same way that REEs can be used if today's current hypothesis are correct.

Some of the other major elements as V, Cr and Mn displays distributional patterns similar to mineral inclusion appearances such as Ilmenite and Rutile. This is explained by substitution in the crystal lattice where 2 or 3+ ions have substituted the Fe or Ti (Vlassopoulos et al., 1993)

Rare earth elements and trace elements

As seen in the mapping there are a significant distribution difference for REEs in the garnet. The HREEs are primarily located in the core, with a large peak towards the outer core boundary, especially for Yb, Dy, Er and to some extent Ho. A second peak that is located at the outer core - rim boundary, is identified by an increase in Dy, Gd and Tb.

The large increase in HREE are attributed to the breakdown of titanite and the release of these elements, which are then incorporated in the garnet itself and other REE bearing inclusions such as allanite. This is explained with the fact that allanite contains more MREEs after titanite breakdown. The timing of which the titanite disappear also concur with the onset of rutile, which indicates that the garnets at the time of forming passed from titanite into rutile's stability field. titanite are generally found at conditions with lower P and T conditions compared to rutile which appears at higher pressure and lower temperatures.

Apatite and allanite are found throughout garnet up until the outer core to core boundary where they both disappear. The disappearance of both apatite and allanite are followed by an enrichment of primarily MREEs such as Gd-Ho in garnet (fig 14). The elements contained in these inclusions can be seen in figures 15 and 16. This peak contains the same elements supposed to be released by the breakdown of both apatite and allanite and can therefore be attributed to the second peak observed in this sample. Similar patterns of REE in mafic apatites are seen in Spandler et al. (2003), which shows that apatites formed from mafic source under epidote-Blueshist conditions, show a large enrichment for just MREE compared to other elements. Which is supported by our own measurements. Our measurements proved that both types of apatite found in the core and the rims of garnet are primary enriched in MREEs. The relative enrichment of REEs in the apatite together with their high abundance yields a good partial explanation to the second peak.

Where the second REE enrichment appears in the garnet monazite appears as the primary REE carrier instead, with apatite-(Cl) appearing just after.

As previously mentioned, the apatites found in the rims of the garnet appear to be more enriched in REEs. This observation could be explained with an increasing metamorphic grade. According to (Bingen et al., 1996) the REEs contained in apatites, increased with higher metamorphic grade.

Allanites are also disappearing before the second peak, and the contained REEs matches perfectly the pattern that are seen in figure 14 at which the second peak appears (Yellow area). At this point monazite becomes the only major REE carrying phase. The monazites measured mirrors the patterns of allanite, the only difference being the HREEs. A reasonable explanation here would be that the allanites occur in the core of garnet where HREEs are more abundant and the monazites occurs in the rim where the overall concentration are lower, which is a result of Rayleigh fractionation with ongoing garnet crystallization. The same explanation is found in Konrad-Schmolke et al., (2008a). Where modeling, recognized both elemental change by mineral reactions, and fractionation during garnet growth.

It is suggested that the monazites are formed at the expense of allanite. This is a reaction supported by several authors such as Giere et al. (2011); Yang and Pattison (2006); Wing et al.

(2003) and the opposite reaction in Finger et al. (2016); Majka and Budzyń (2006); and others. The phosphorus needed for the reaction would in this case come from the breakdown of apatite which occurs simultaneously in this case, which is also supported by (Wing et al., 2003; Janots et al., 2008).

(Janots et al., 2008; formula 7) describes on possible reaction as follows –

$$\text{“}Allanite + Apatite + Al - Fe - Mg\ phases\ (1) = > Monazite + anorthite + Al - Fe - Mg\ phases\ (2)\text{”}$$

Where the Al-Fe-Mg phases are believed to be incorporated into garnet and plagioclase in his work, which would be the case here as well. There are increasing iron content in the garnet and plagioclase appearing in the matrix at the time of monazite growth which would here correspond to area C-D in the works of (Martin and Tartarotti, 1989)

Furthermore, the occurrence of monazite overgrowth on allanites have been observed in the same sample (figure A2 -Appendices), which further supports the claim that the monazites in this sample are a product from apatite and allanite breakdown, with phosphorus coming from apatite.

The disappearance of apatite and allanite in the garnet are explained with the fact that we leave their stability field and enter the stability field for monazites at the rim. Monazites stability field can occur at higher pressure and temperature compared to both allanite and apatite, and the breakdown of these minerals can according to Giere et al. (2011) form monazite as a replacement product.

Several articles also discuss the importance of Ca in relation to the stability of allanite. Systems with high Ca concentrations extends the stability field of allanite to higher P-T conditions. (Janots et al., 2007). In this sample, there could be made a small correlation to the lack of Ca in garnet and the disappearing allanite. As Ca concentration in garnet decreases rapidly before the onset of monazite, as seen in the mapping images. However, this is beyond the scope of this study.

P-T path and mineral assemblages

As previously shown, the metamorphic pathway of the samples from Saint Marcel is counterclockwise. The different areas marked within the stability of monazite/allanite series (Janots et al., 2007), are estimated Pressure and temperature windows for certain mineral assemblages found in the sample (first mentioned by Tartarotti, 1989). The different areas can

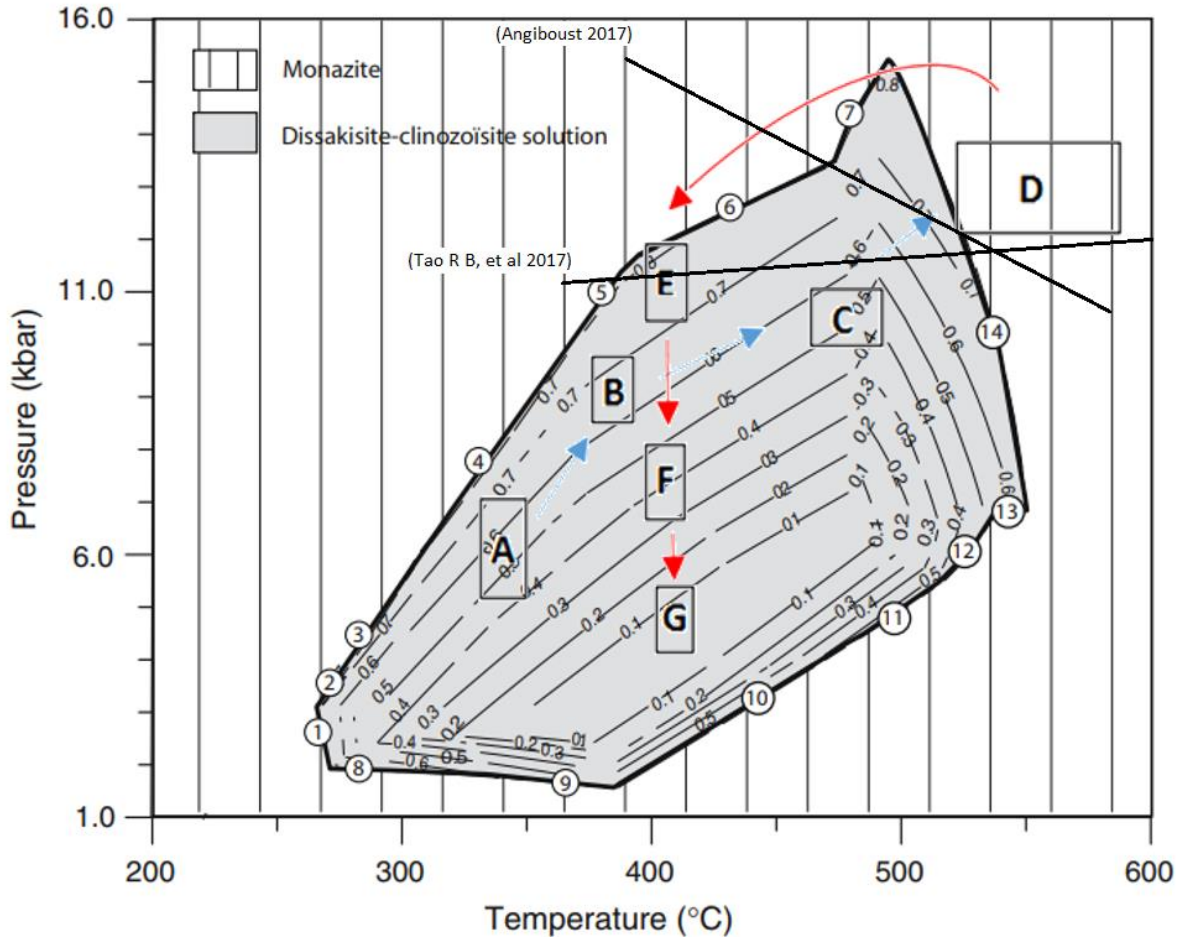

Figure 17. Allanite – Monazites relative stability field as modeled by (Janots et al 2007) with overlay of the PT pathway of the sample, together with the transition between Titanite and Rutile as seen in the works from Angiboust 2017 and Tao et al 2017)

be interpreted with the help of the garnet itself, as the mineral assemblages are preserved for this sample.

The observed transition from titanite to rutile and for allanite to monazite in the garnet fig 17 (C-D area), agree with modeled result from both Angiboust and Harlow (2017), and Tao et al. (2017). This strengthens the thesis, that these reactions are the main reason for the changing REE concentration seen in the garnet.

Conclusions

The first REE peak in the sample is the result of titanite breaking down and rutile appearing as the major titanium face. As rutile do not contain any REEs they instead end up in other compatible minerals, such as garnet and allanite in this case. Therefore, we see an increase in REEs in both the garnet and in the allanite inclusions growing in the garnet after the titanite breakdown.

The second peak are the result of a combination of reactions, where apatite-F and allanite are replaced by monazite and apatite-Cl. The combined molar abundance of apatite and allanite exceeds the molar abundance of monazite, and we therefore see a peak in REEs where monazite appears.

Breakdown of REE bearing facies responsible for the rapid increase of REE in garnet. A decrease in REE bearing minerals also contribute to the increase of REE in garnet despite higher molar abundance

With further research in this topic it could in the future, be possible to interpret relict mineral reactions using REE patterns, as diffusion processes do not affect them as much as major elements. This is very useful as mineral chemistry and assemblages are usually altered or completely replaced from its original composition.

References

Anders, E., & Grevesse, N. (1989). Abundances of the elements: Meteoritic and solar. Geochimica et Cosmochimica Acta, 53(1), 197-214.

Angiboust, S., & Harlov, D. (2017). Ilmenite breakdown and rutile-titanite stability in metagranitoids: Natural observations and experimental results. *American Mineralogist, 102*(8), 1696-1708.

Babist, J., M. R. Handy, M. Konrad-Schmolke, and K. Hammerschmidt. "Precollisional, multistage exhumation of subducted continental crust: The Sesia Zone, western Alps." *Tectonics* 25, no. 6 (2006).

Bingen, B., Demaiffe, D., & Hertogen, J. (1996). Redistribution of rare earth elements, thorium, and uranium over accessory minerals in the course of amphibolite to granulite facies metamorphism: the role of Apatite and Monazite in orthogneisses from southwestern Norway. *Geochimica et Cosmochimica Acta*, *60*(8), 1341-1354.

Carlson, W. D. (2002). Scales of disequilibrium and rates of equilibration during metamorphism. *American Mineralogist*, *87*(2-3), 185-204.

Carlson, W. D. (2012). Rates and mechanism of Y, REE, and Cr diffusion in garnet. *American Mineralogist, 97*(10), 1598-1618.

Carlson, W. D., Gale, J. D., & Wright, K. (2014). Incorporation of Y and REEs in aluminosilicate garnet: Energetics from atomistic simulation. *American Mineralogist*, *99*(5-6), 1022-1034.

Chakraborty, S. (2006). Diffusion modeling as a tool for constraining timescales of evolution of metamorphic rocks. *Mineralogy and Petrology*, *88*(1-2), 7-27.

Dal Piaz, G. V. (1999). The Austroalpine-Piedmont nappe stack and the puzzle of Alpine Tethys. *Memorie di Scienze Geologiche*, *51*(1), 155-176.

Duchêne, S., Blichert-Toft, J., Luais, B., Télouk, P., Lardeaux, J. M., & Albarede, F. (1997). The Lu–Hf dating of garnets and the ages of the Alpine high-pressure metamorphism. *Nature*, *387*(6633), 586-589.

Dragovic, B., Samanta, L. M., Baxter, E. F., & Selverstone, J. (2012). Using garnet to constrain the duration and rate of water-releasing metamorphic reactions during subduction: An example from Sifnos, Greece. *Chemical Geology*, *314*, 9-22.

Finger, F., Krenn, E., Schulz, B., Harlov, D., & Schiller, D. (2016). “Satellite Monazites” in polymetamorphic basement rocks of the Alps: Their origin and petrological significance. American Mineralogist, 101(5), 1094-1103.

George, F. R., Gaidies, F., & Boucher, B. (2018). Population-wide garnet growth zoning revealed by LA-ICP-MS mapping: implications for trace element equilibration and syn-kinematic deformation during crystallisation. *Contributions to Mineralogy and Petrology*, *173*(9), 74.

Gieré, R., Rumble, D., Günther, D., Connolly, J., & Caddick, M. J. (2011). Correlation of growth and breakdown of major and accessory minerals in metapelites from Campolungo, Central Alps. Journal of Petrology, 52(12), 2293-2334.

Griffin, W. L., & Brueckner, H. K. (1980). Caledonian Sm–Nd ages and a crustal origin for Norwegian eclogites. *Nature*, *285*(5763), 319-321.

Hauri, E. H., Wagner, T. P., & Grove, T. L. (1994). Experimental and natural partitioning of Th, U, Pb and other trace elements between garnet, clinopyroxene and basaltic melts. *Chemical Geology*, *117*(1-4), 149-166.

Janots, E., Brunet, F., Goffé, B., Poinssot, C., Burchard, M., & Cemič, L. (2007). Thermochemistry of Monazite-(La) and dissakisite-(La): implications for Monazite and Allanite stability in metapelites. Contributions to Mineralogy and Petrology, 154(1), 1-14.

Janots, E., Engi, M., Berger, A., Allaz, J., Schwarz, J. O., & Spandler, C. (2008). Prograde metamorphic sequence of REE minerals in pelitic rocks of the Central Alps: implications for allanite–monazite–xenotime phase relations from 250 to 610 C. *Journal of Metamorphic Geology*, *26*(5), 509-526.

Jamtveit, B., & Hervig, R. L. (1994). Constraints on transport and kinetics in hydrothermal systems from zoned garnet crystals. *Science*, *263*(5146), 505-508.

Jochum, K. P., Willbold, M., Raczek, I., Stoll, B., & Herwig, K. (2005). Chemical Characterisation of the USGS Reference Glasses GSA-1G, GSC-1G, GSD-1G, GSE-1G, BCR-2G, BHVO-2G and BIR-1G Using EPMA, ID-TIMS, ID-ICP-MS and LA-ICP-MS. *Geostandards and Geoanalytical Research*, *29*(3), 285-302.

Kohn, M. J. (2009). Models of garnet differential geochronology. *Geochimica et Cosmochimica Acta*, *73*(1), 170-182.

Kohn, M. J. (2017). Titanite petrochronology. Reviews in Mineralogy and Geochemistry, 83(1), 419-441.

Konrad-Schmolke, M., Babist, J., Handy, M. R., & O'brien, P. J. (2006). The physico-chemical properties of a subducted slab from garnet zonation patterns (Sesia Zone, Western Alps). Journal of Petrology, 47(11), 2123-2148.

Konrad-Schmolke, M., O'Brien, P. J., de Capitani, C., & Carswell, D. A. (2008a). Garnet growth at high-and ultra-high pressure conditions and the effect of element fractionation on mineral modes and composition. *Lithos*, *103*(3-4), 309-332.

Konrad-Schmolke, M., Zack, T., O'Brien, P. J., & Jacob, D. E. (2008b). Combined thermodynamic and rare earth element modelling of garnet growth during subduction: examples from ultrahigh-pressure eclogite of the Western Gneiss Region, Norway. Earth and Planetary Science Letters, 272(1-2), 488-498.

Kohn, M. J., & Spear, F. S. (1991). Error propagation for barometers; 1, Accuracy and precision of experimentally located end-member reactions. *American Mineralogist*, *76*(1-2), 128-137

Kotková, J., & Harley, S. L. (2010). Anatexis during high-pressure crustal metamorphism: Evidence from garnet–whole-rock REE relationships and zircon–rutile Ti–Zr thermometry in leucogranulites from the Bohemian Massif. *Journal of Petrology*, *51*(10), 1967-2001.

Li, B., Ge, J., & Zhang, B. (2018). Diffusion in garnet: a review. *Acta Geochimica*, *37*(1), 19-31

Majka, J., & Budzyń, B. (2006). Monazite breakdown in metapelites from Wedel Jarlsberg Land, Svalbard—preliminary report. Mineralogia, 37(1), 61-69.

Martin, S., & KLENAST, J. (1987). The HP-LT manganiferous Quartzites of Praborna, Piemonte ophiolite nappe, Italian western Alps. Schweizerische Mineralogische und Petrographische Mitteilungen, 67(3), 339-360.

Martin, S., Rebay, G., Kienast, J.-R., & Mével., C. (2008). An eclogitised oceanic palaeo-hydrothermal field from the St. Marcel Valley (Italian Western Alps). Ofioliti, 33(1), 49–63.

Martin, S., & Tartarotti, P. (1989). Polyphase HP metamorphism in the ophiolitic glaucophanites of the lower St. Marcel Valley (Aosta valley).

Moore, S. J., Carlson, W. D., & Hesse, M. A. (2013). Origins of yttrium and rare earth element distributions in metamorphic garnet. *Journal of Metamorphic Geology*, *31*(6), 663-689.

Moyen, J. F. (2009). High Sr/Y and La/Yb ratios: the meaning of the "adakitic signature". *Lithos*, *112*(3-4), 556-574.

Paquin, J., & Altherr, R. (2001). New constraints on the P–T evolution of the Alpe Arami garnet peridotite body (Central Alps, Switzerland). *Journal of Petrology*, *42*(6), 1119-1140.

Paquin, J., Altherr, R., & Ludwig, T. (2004). Li–Be–B systematics in the ultrahigh-pressure garnet peridotite from Alpe Arami (Central Swiss Alps): implications for slab-to-mantle wedge transfer. *Earth and Planetary Science Letters*, *218*(3-4), 507-519.

Paton, C., Hellstrom, J., Paul, B., Woodhead, J., & Hergt, J. (2011). Iolite: Freeware for the visualisation and processing of mass spectrometric data. *Journal of Analytical Atomic Spectrometry*, *26*(12), 2508-2518.

Pearce, N. J., Perkins, W. T., Westgate, J. A., Gorton, M. P., Jackson, S. E., Neal, C. R., & Chenery, S. P. (1997). A compilation of new and published major and trace element data for NIST SRM 610 and NIST SRM 612 glass reference materials. Geostandards Newsletter, 21(1), 115-144.

Raimondo, T., Payne, J., Wade, B., Lanari, P., Clark, C., & Hand, M. (2017). Trace element mapping by LA-ICP-MS: assessing geochemical mobility in garnet. *Contributions to Mineralogy and Petrology*, *172*(4), 17.

Rubatto, D., & Hermann, J. (2003). Zircon formation during fluid circulation in eclogites (Monviso, Western Alps): implications for Zr and Hf budget in subduction zones. *Geochimica et Cosmochimica Acta*, *67*(12), 2173-2187.

Schmidt, A., Weyer, S., Mezger, K., Scherer, E. E., Xiao, Y., Hoefs, J., & Brey, G. P. (2008). Rapid eclogitisation of the Dabie–Sulu UHP terrane: constraints from Lu–Hf garnet geochronology. *Earth and Planetary Science Letters*, *273*(1-2), 203-213.

Skora, S., Baumgartner, L. P., Mahlen, N. J., Johnson, C. M., Pilet, S., & Hellebrand, E. (2006). Diffusion-limited REE uptake by eclogite garnets and its consequences for Lu–Hf and Sm–Nd geochronology. *Contributions to Mineralogy and Petrology*, *152*(6), 703-720.

Spandler, C., Hermann, J., Arculus, R., & Mavrogenes, J. (2003). Redistribution of trace elements during prograde metamorphism from lawsonite blueschist to eclogite facies; implications for deep subduction-zone processes. Contributions to Mineralogy and Petrology, 146(2), 205-222.

Spear, F. S., & Menard, T. (1989). Program GIBBS; a generalized Gibbs method algorithm. *American Mineralogist*, *74*(7-8), 942-943.

Spear, F. S., & Daniel, C. G. (2001). Diffusion control of garnet growth, Harpswell Neck, Maine, USA. *Journal of metamorphic Geology*, *19*(2), 179-195.

Lin, M. L., & Tan, P. H. (2019). Ultralow-Frequency Raman Spectroscopy of Two-dimensional Materials. In *Raman Spectroscopy of Two-Dimensional Materials* (pp. 203-230). Springer, Singapore.

Tartarotti, P., Martin, S., Monopoli, B., Benciolini, L., Schiavo, A., Campana, R., & Vigni, I. (2017). Geology of the Saint-Marcel valley metaophiolites (Northwestern Alps, Italy). Journal of Maps, 13(2), 707-717.

Tracy, R. J., Robinson, P., & Thompson, A. B. (1976). Garnet composition and zoning in the determination of temperature and pressure of metamorphism, central Massachusetts. *American mineralogist*, *61*(7-8), 762-775.

Ubide, T., McKenna, C. A., Chew, D. M., & Kamber, B. S. (2015). High-resolution LA-ICP-MS trace element mapping of igneous minerals: In search of magma histories. *Chemical Geology*, *409*, 157-168.

Vlassopoulos, D., Rossman, G. R., & Haggerty, S. E. (1993). Coupled substitution of H and minor elements in Rutile and the implications of high OH contents in Nb-and Cr-rich Rutile from the upper mantle. American Mineralogist, 78(11-12), 1181-1191.

Wing, B. A., Ferry, J. M., & Harrison, T. M. (2003). Prograde destruction and formation of Monazite and Allanite during contact and regional metamorphism of pelites: petrology and geochronology. Contributions to Mineralogy and petrology, 145(2), 228-250.

Whitehouse, M. J., & Platt, J. P. (2003). Dating high-grade metamorphism—constraints from rare-earth elements in zircon and garnet. *Contributions to Mineralogy and Petrology*, *145*(1), 61-74.

Yang, P., & Pattison, D. (2006). Genesis of Monazite and Y zoning in garnet from the Black Hills, South Dakota. Lithos, 88(1-4), 233–253. doi:10.1016/j.lithos.2005.08.012

Appendix

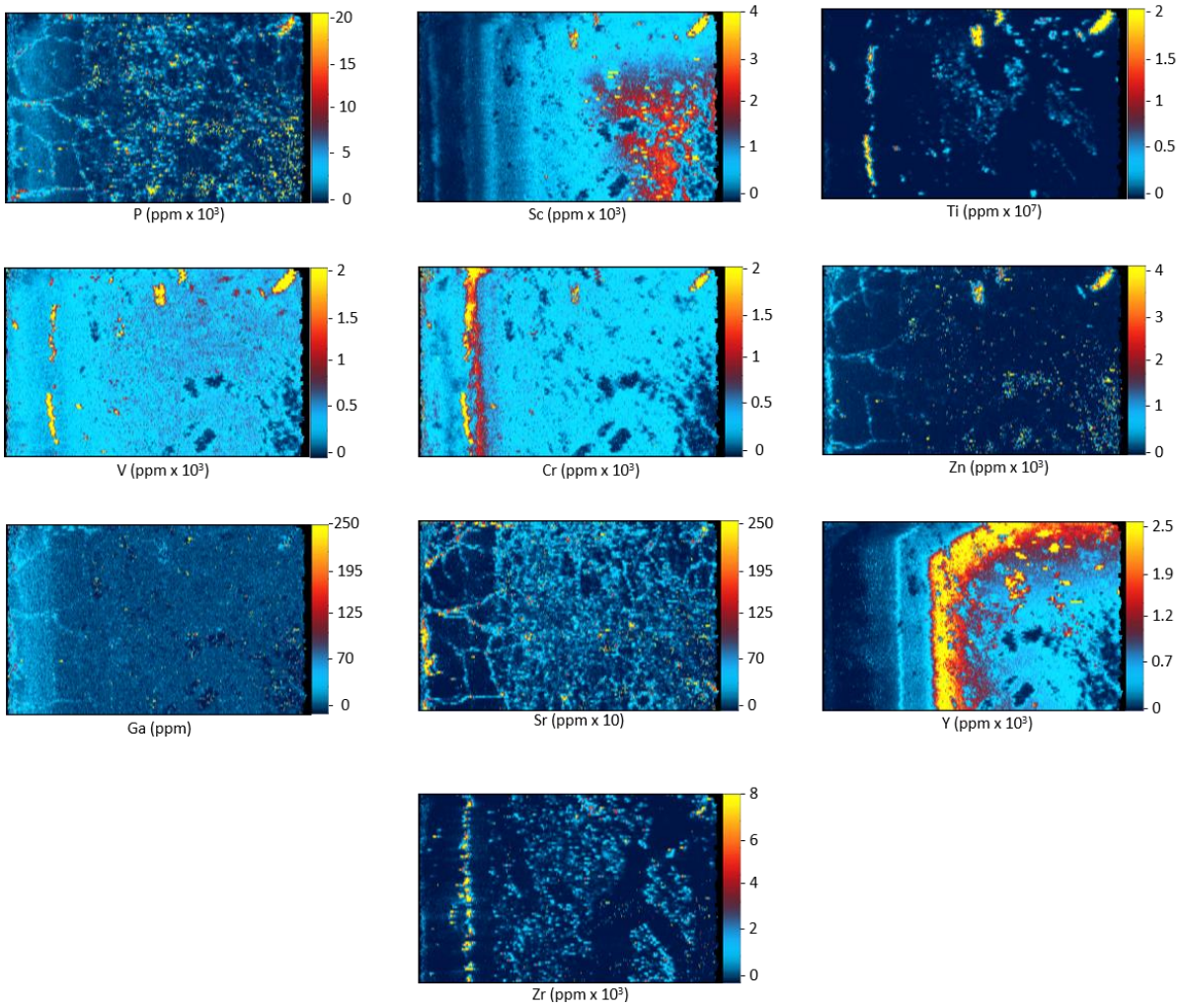

Figure A1 - Major elements and trace elements incorporated in inclusions and the structure of garnet. All maps have been adjusted so that zonation and certain enrichments of these elements are as evident as possible. Note that the direction of laser travel is from right to left in images.

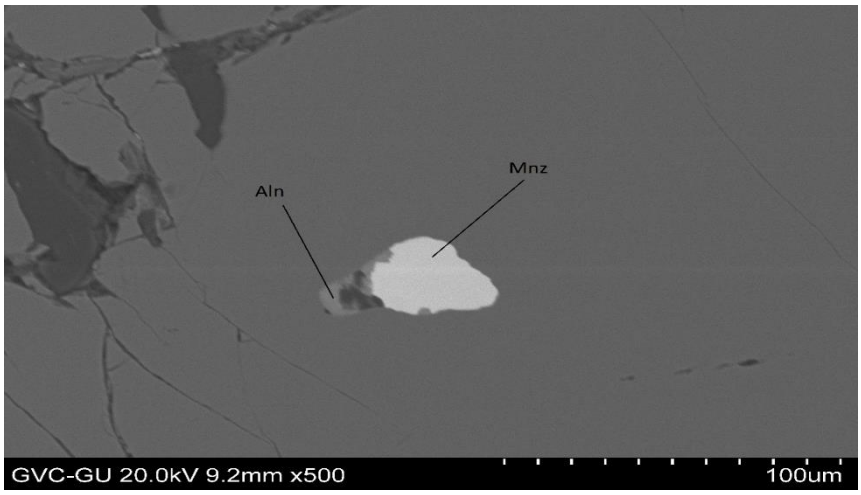

Figure A2 - Allanite overgrown by Monazite at the outer core, zone 2-3 - rim boundary.